Oxygen nonstoichiometry and thermodynamic characterization of Zr doped ceria in the 1573-1773 K temperature range

Journal Article

Author(s):
Takacs, Michael; Scheffe, Jonathan R.; Steinfeld, Aldo

Publication date:
2015-03-28

Permanent link:
https://doi.org/10.3929/ethz-b-000099908

Originally published in:
Physical Chemistry Chemical Physics 17(12), https://doi.org/10.1039/c4cp04916k

Funding acknowledgement:
320541 - Solar thermochemical production of fuels (EC)

PCCP

PAPER

View Article Online
View Journal | View Issue

Cite this: *Phys. Chem. Chem. Phys.*, 2015, **17**, 7813

Oxygen nonstoichiometry and thermodynamic characterization of Zr doped ceria in the 1573–1773 K temperature range†

M. Takacs, J. R. Scheffe*‡ and A. Steinfeld

Received 27th October 2014,
Accepted 12th February 2015

DOI: 10.1039/c4cp04916k

www.rsc.org/pccp

This work encompasses the thermodynamic characterization and critical evaluation of Zr^{4+} doped ceria, a promising redox material for the two-step solar thermochemical splitting of H_2O and CO_2 to H_2 and CO. As a case study, we experimentally examine 5 mol% Zr^{4+} doped ceria and present oxygen nonstoichiometry measurements at elevated temperatures ranging from 1573 K to 1773 K and oxygen partial pressures ranging from 4.50×10^{-3} atm to 2.3×10^{-4} atm, yielding higher reduction extents compared to those of pure ceria under all conditions investigated, especially at the lower temperature range and at higher p_{O_2}. In contrast to pure ceria, a simple ideal solution model accounting for the formation of isolated oxygen vacancies and localized electrons accurately describes the defect chemistry. Thermodynamic properties are determined, namely: partial molar enthalpy, entropy, and Gibbs free energy. In general, partial molar enthalpy and entropy values of Zr^{4+} doped ceria are lower. The equilibrium hydrogen yields are subsequently extracted as a function of the redox conditions for dopant concentrations as high as 20%. Although reduction extents increase greatly with dopant concentration, the oxidation of Zr^{4+} doped ceria is thermodynamically less favorable compared to pure ceria. This leads to substantially larger temperature swings between reduction and oxidation steps, ultimately resulting in lower theoretical solar energy conversion efficiencies compared to ceria under most conditions. In effect, these results point to the importance of considering oxidation thermodynamics in addition to reduction when screening potential redox materials.

Introduction

Solar-driven thermochemical redox cycles utilizing nonstoichiometric metal oxides are capable of splitting H_2O and CO_2 to produce H_2 and CO (syngas), the precursors to the catalytic synthesis of conventional liquid fuels.[1,2] Ceria (CeO_2) is currently considered a state-of-the-art material because it displays rapid oxidation and reduction kinetics and is morphologically stable over a range of temperatures and reduction extents.[3] The two-step thermochemical cycle using CeO_2 as reactive intermediate is represented by:

Reduction at T_{red}:

$$CeO_2 = CeO_{2-\delta} + \frac{\delta}{2}O_2 \qquad (1)$$

Oxidation at T_{ox}:

$$CeO_{2-\delta} + \alpha H_2O + \beta CO_2 = CeO_2 + \alpha H_2 + \beta CO \qquad (2)$$

where $\alpha + \beta = \delta$. In the endothermic first step, eqn (1), ceria is reduced typically under an atmosphere of low oxygen partial pressure (p_{O_2}) at elevated temperatures, generally $T_{red} > 1573$ K, where the process heat is delivered by concentrated solar energy. In an exothermic second step, eqn (2), the reduced ceria is re-oxidized with H_2O or CO_2 at lower temperatures, generally $T_{ox} < 1573$ K, to produce H_2 or CO. The oxygen nonstoichiometry (δ) achieved during reduction depends strongly on T_{red} and p_{O_2} in the system[4,5] and is directly related to the maximum amount of H_2/CO capable of being produced per mole ceria in the second step. As ceria is not consumed within the process, the net reactions are $H_2O = H_2 + 1/2O_2$ and $CO_2 = CO + 1/2O_2$. In contrast to direct thermolysis, two-step redox cycles bypass the separation of fuel and O_2 at high temperatures. Contrary to photochemical processes, solar thermochemical processes utilize the entire solar spectrum and thus offer a thermodynamically favorable path towards fuel production.

Since the reduction extent of ceria is generally lower than those obtained by other appropriate redox materials (*e.g.* ferrite,

Department of Mechanical and Process Engineering, ETH Zurich, 8092 Zurich, Switzerland

† Electronic supplementary information (ESI) available: XRD patterns and SEM images. See DOI: 10.1039/c4cp04916k

‡ Present address: Dept. of Mechanical and Aerospace Engineering, University of Florida, 231 MAE-A Building, P. O. Box 116250, Gainsville, FL 32611-6250, USA. E-mail: jscheffe@ufl.edu; Tel: +1-352-352-0839.

zinc oxide), its specific fuel production per mass is low.[3,6] This has a direct implication on efficiencies because they are largely dictated by the ratio of fuel produced to that of the thermal energy required to heat the oxide between oxidation and reduction steps.[7] Therefore, in an attempt to increase reduction extents, 4+ valence dopants such as Zr^{4+} [8–12] and Hf^{4+} [8,13] are often introduced into the ceria lattice. Cycling studies of Zr^{4+} doped ceria have shown favorable reduction extents during reduction, but slower re-oxidation kinetics with CO_2[8,11] or H_2O[14] were observed compared to pure ceria. Scheffe *et al.*[8] showed that reduction extents of Zr^{4+} and Hf^{4+} doped ceria increase with increasing dopant concentration up to 15 mol% whereas re-oxidation is generally slower than pure ceria but appeared to be strongly dependent on available surface area. Call *et al.*[11] concluded that reduction extents increase for dopant concentrations up to 22.5 mol%. Le Gal *et al.*[14] observed increasing oxygen release up to dopant concentrations of 25 mol% Zr^{4+} but the reduced forms could not be completely re-oxidized with steam at 1323 K. In summary, most of the above studies report consistent results, namely increasing reduction extents with 4+ valence dopant concentration but at the same time slower oxidation kinetics. Comparison between different works is difficult because the detailed experimental conditions (*e.g.* particle size) are generally not reported or controlled, and it is not clear from these studies whether thermodynamic limitations or inherent kinetics hinder the rates.

Thermodynamic studies have been performed at temperatures below the range of interest for thermochemical cycles. For example, Kuhn *et al.*[10] reported oxygen nonstoichiometric measurements of Zr^{4+} doped ceria at $T \leq 1273$ K and dopant concentrations between 5 and 80 mol%. Shah *et al.*[15] reported measurements for Zr^{4+} concentrations of 19 and 75 mol% at $T \leq 1173$ K and $p_{O_2} \leq 10^{-10}$ atm. Very recently, Hao *et al.*[12] published nonstoichiometric measurements at higher temperatures for Zr^{4+} dopant concentrations up to 20 mol% in the range T = 873 K to 1763 K and $p_{O_2} \approx 10^{-27}$ atm to 1 atm. All three studies[10,12,15] indicate a higher oxygen nonstoichiometry of doped ceria compared to pure ceria, which increases with increasing dopant concentration up to 20 mol%, and derive enthalpy and entropy values slightly lower than those for pure ceria.[4,5,16,17]

In this work, we evaluate the thermochemical performance of Zr^{4+} doped ceria by using 5 mol% as a case study. Oxygen nonstoichiometry is reported in the operation range of solar reactors (1573 K $\leq T_{red} \leq$ 1773 K, 2.3×10^{-4} atm $< p_{O_2} <$ 4.50×10^{-3} atm) for 5 mol% Zr^{4+} doped ceria (CZO_5) and undoped ceria (CeO_2). We develop appropriate defect models to describe the defect chemical equilibria and in turn extract partial molar thermodynamic properties (Δh_O, Δs_O and Δg_O). From such data coupled with thermodynamic data from the literature, we determine equilibrium hydrogen yields and theoretical solar-to-fuel energy conversion efficiencies for dopant concentrations as high as 20 mol%. This analysis allows a straightforward and quantitative methodology for evaluating the potential of Zr^{4+} doped ceria used in solar thermochemical redox cycles.

Experimental section

Synthesis technique and sample characterization

5 mol% Zr^{4+} doped CeO_2 (CZO_5) powder was synthesized by sol–gel method as described by Scheffe *et al.*[8] Briefly, $Ce(NO_3)_3 \cdot 6H_2O$ (Aldrich, catalog number 238538), $ZrO(NO_3)_2 \cdot 6.3H_2O$ (Aldrich, catalog number 243493) and dry citric acid (Merck, catalog number 818707) in aqueous solution were used to carry out the synthesis. The ratio of the metal cations to the citric acid was 1 : 1.5. CeO_2 powder was purchased from a commercial distributor (Aldrich, catalog number 211575). CeO_2 and CZO_5 powders were uniaxially cold-pressed at 5 tons and sintered at 1873 K under air atmosphere for 5 hours into ~1250 mg dense cylindrical pellets. The approximate dimensions after sintering were 7 mm diameter and 5 mm height. The CZO_5 dopant concentration was measured by inductively coupled plasma mass spectrometry (ICP-MS) analysis and was 4.5 mol%. Powder X-ray diffraction (XRD) was performed in the Bragg Brentano geometry using Cu Kα radiation (Philips, PANalytical/X′Pert MPD/DY636, λ = 1.5406 Å, 2Θ = 20–100°, 0.01° s^{-1} scan rate, 45 kV/20 mA output). Scanning electron microscopy (SEM) of the dense pellets were conducted on a TM-1000 Microscope (Hitachi, 15 kV accelerating voltage). XRD patterns and SEM images are shown in ESI.†

Experimental measurements

Oxygen nonstoichiometry (δ) was measured using a thermogravimetric analyzer (TGA, Setaram Setsys Evolution). Samples were suspended to the scale with a custom-made platinum hook to ensure good exposure to the purge gas and eliminate gas diffusion limitations. Special care was taken to ensure that reduction and oxidation reactions were not limited by gaseous mass transfer but by solid-state diffusion and/or surface reactions. The p_{O_2} of the surrounding gas atmosphere was controlled by mixing Ar (Messer, Argon 4.6) with an O_2–Ar mixture (Messer, 0.5% O_2 5.0 in Ar 5.0). Gases were mixed with electronic mass flow controllers (Brooks, Model 5850TR, accuracy ±1%) with a constant total flow rate of 200 ml min^{-1}. The gas species and concentrations at the outlet were monitored by mass spectrometry (Pfeiffer Vacuum, OmniStar GSD 320). Temperature was varied between 1573 K and 1773 K and p_{O_2} between 4.50×10^{-3} atm and 2.3×10^{-4} atm. In all measurements, the sample mass (m_s) was equilibrated at a constant temperature and p_{O_2}. Following each equilibrium measurement, the p_{O_2} was rapidly changed by adapting the O_2–Ar gas mixture, resulting in a temporal weight change of the sample due to evolving or uptaking of oxygen until a new equilibrium was reached. To correct for buoyancy, blank runs were performed with Al_2O_3 sintered pellets of same dimensions. An additional correction was applied for a small amount of sample sublimation (<0.04 wt%) observed above 1723 K.

Oxygen nonstoichiometry

An exemplary experiment showing the dynamics of the reduction (decreasing p_{O_2}) and oxidation (increasing p_{O_2}) of CZO_5 and CeO_2 at 1573 K and 1773 K is shown in Fig. 1(a). Initially, their

weights were stabilized at a constant p_{O_2}, followed by a rapid p_{O_2} decrease to initiate reduction. After stabilization at the new m_s, p_{O_2} is increased back to its initial value to commence oxidation. At 1573 K, the reduction and oxidation of CZO_5 are noticeably slower than those of CeO_2. However, at 1773 K, the kinetic rates are similar for both materials. If surface reactions are assumed not to be limiting – a reasonable assumption at these length scales – this would imply that the activation energy for ambipolar diffusion is higher in the case of CZO_5.

Fig. 1(b) shows the mass change in wt% of CeO_2 and CZO_5 as a function of time for T = 1673 K for a broader range of p_{O_2} and Fig. 1(c) shows all the reduction and oxidation runs over all temperatures and p_{O_2}. Samples were heated to 5 different set point temperatures followed by isothermal reduction and oxidation by stepwise changing p_{O_2}. As seen, CZO_5 released more oxygen than CeO_2 under all measurement conditions. The much slower oxidation of CZO_5 at 1073 K agrees well with the observation that its activation energy for ambipolar diffusion is higher than CeO_2 (*cf.* Fig. 1(a) and discussion above). A total sublimated mass of 0.40 mg and 0.32 mg at 1773 K was observed for CeO_2 and CZO_5, respectively.

Oxygen nonstoichiometry is calculated according to:

$$\delta = \Delta m_s \cdot \frac{M_s}{M_O} \tag{3}$$

where Δm_s is the relative weight loss at equilibrium, M_s is the molar mass of the sample and M_O the molar mass of O. Measured δ *versus* p_{O_2} of CeO_2 and CZO_5 for all temperatures investigated are shown in Fig. 2(a) and (b), respectively. Open symbols show δ measurements of this work whereas literature data are shown by closed symbols (Panlener *et al.*[4]) and crossed symbols (Iwasaki *et al.*[18]). Lines indicate defect models used to describe δ, presented in the following section. As seen, δ of CZO_5 is higher over the whole measurement range investigated compared to CeO_2. Improvement in oxygen release is highest at low T_{red} and high p_{O_2}. For example, at T = 1623 K and $p_{O_2} \approx 4.50 \times 10^{-3}$ atm, the improvement is almost 90% per mole of oxide (δ = 0.010 for CZO_5 and δ = 0.0055 for CeO_2) and around 27% at T = 1773 K and $p_{O_2} \approx 2.3 \times 10^{-4}$ atm (δ = 0.042 for CZO_5 and δ = 0.033 for CeO_2). Nonstoichiometry of CZO_5 at 1573 K is not shown because the sample weight did not equilibrate completely within the allotted time due to slower kinetics. δ values of pure CeO_2 measured in this work are slightly higher than the values reported in literature,[4,18] especially towards higher p_{O_2}. The reason for the discrepancy is not clear but may be related to sample impurities and sublimation. Panlener *et al.*[4] performed oxygen nonstoichiometry measurements based on thermogravimetric analysis over a broad range of p_{O_2} from 0.01 atm to 10^{-23} atm between 873 K and 1773 K while Iwasaki *et al.*[18] performed measurements only at temperatures up to 1573 K.

Defect model

Defect models were used to describe the chemical equilibria of both CeO_2 and CZO_5. For small reduction extents (as small as δ = 0.01 for pure ceria and higher with dopant type and dopant concentration[19]) the reduction of ceria and doped ceria can be described in Kröger–Vink notation as:

$$2Ce_{Ce}^{\times} + O_O^{\times} = 2Ce_{Ce}' + V_O^{\bullet\bullet} + \frac{1}{2}O_2 \tag{4}$$

where oxygen atoms on oxygen lattice sites ($O_O^{\times}$) and cerium on cerium lattice sites ($Ce_{Ce}^{\times}$) are in equilibrium with gaseous oxygen, doubly ionized oxygen vacancies ($V_O^{\bullet\bullet}$) and electrons localized on cerium lattice sites (Ce_{Ce}'). Assuming there are no

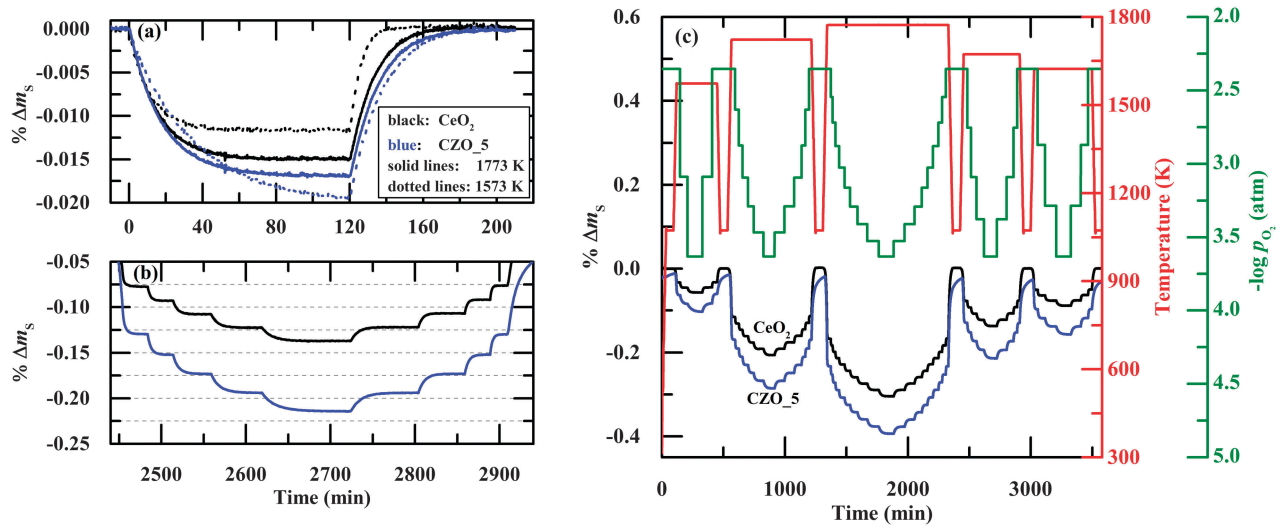

Fig. 1 (a) Mass change in wt% as a function of time for the reduction and oxidation of CeO_2 (black) and CZO_5 (blue) at T = 1773 K where p_{O_2} was changed between 3.0 × 10^{-4} atm and 2.3 × 10^{-4} atm (solid lines) and at T = 1573 K where p_{O_2} was changed between 8.1 × 10^{-4} atm and 2.3 × 10^{-4} atm (dotted lines). (b) Mass change in wt% as a function of time for the reduction and oxidation runs of CeO_2 (black) and CZO_5 (blue) at T = 1673 K and O_2 partial pressure range p_{O_2} = 4.50 × 10^{-3}–2.3 × 10^{-4} atm. (c) Mass change in wt% as a function of time for all the reduction and oxidation runs of CeO_2 and CZO_5 in the temperature range T = 1573–1773 K and O_2 partial pressure range p_{O_2} = 4.50 × 10^{-3}–2.3 × 10^{-4} atm.

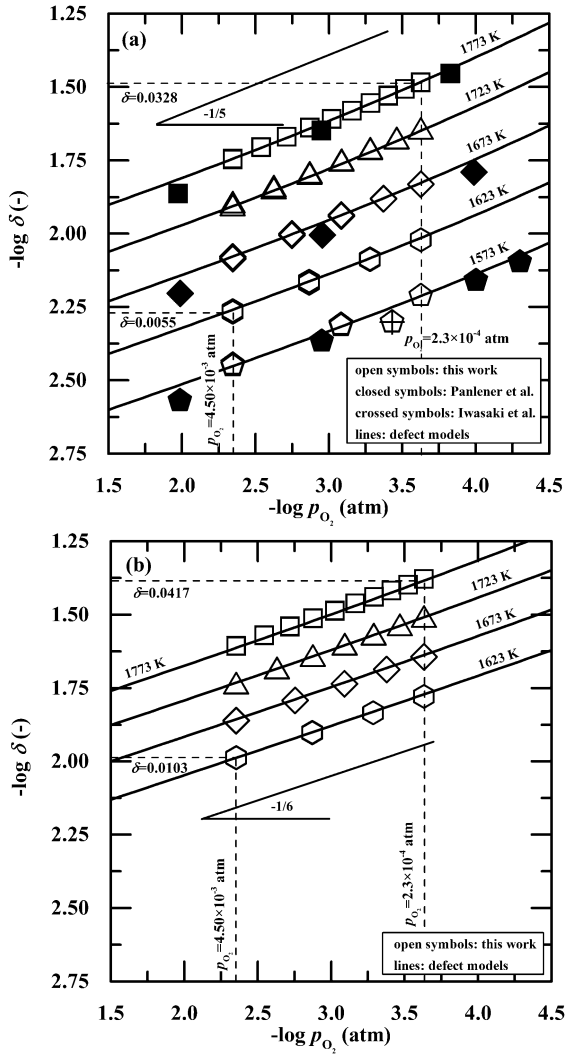

Fig. 2 Measured δ (open symbols) of CeO_2 (a) and CZO_5 (b) for T = 1573 K to 1773 K and p_{O_2} = 4.50 × 10^{-3} atm to 2.3 × 10^{-4} atm and a comparison to literature data: Panlener *et al.*:[4] closed symbols, Iwasaki *et al.*:[18] crossed symbols. Lines indicate defect models used to describe δ.

cluster formations between the various defects, δ can be described by:[10,20]

$$\delta = \text{constant} \cdot p_{O_2}{}^{-1/6}\big|_{T=\text{const.}} \tag{5}$$

which implies a slope of −1/6 when plotting $\log\delta$ *versus* $\log p_{O_2}$.

For larger deviations from stoichiometry, the formation of oxygen vacancy–polaron associations $\left(Ce'_{Ce}V_O^{\bullet\bullet}Ce'_{Ce}\right)^{\times}$ should be accounted for, and is described as:

$$2Ce'_{Ce} + V_O^{\bullet\bullet} = \left(Ce'_{Ce}V_O^{\bullet\bullet}Ce'_{Ce}\right)^{\times} \tag{6}$$

Assuming all defects form associations according to eqn (6),[20]

$$\delta = \text{constant} \cdot p_{O_2}{}^{-1/2}\big|_{T=\text{const.}} \tag{7}$$

As seen in the case of CeO_2 (Fig. 2(a)), the slope of $\log\delta$ *vs.* $\log p_{O_2}$ best describing the data is close to −1/5, indicating that eqn (5) cannot adequately describe its defect equilibria, in agreement with previous investigations.[4,16,19,21,22] A slope of −1/5 indicates that a combination of both defect models (eqn (4) and (6)) is needed to accurately describe ceria's defect chemistry, as evidenced by Otake *et al.*[19] who showed that the isolated defect model is only valid for very low nonstoichiometries ($\delta < 0.01$). A slope of −1/6, on the other hand adequately describes the data of CZO_5 over the entire measurement range. This is consistent with observations of 3+ valence dopants such as Sm^{3+},[22,23] Gd^{3+}[22,24,25] and Y^{3+},[19] but in such cases much higher concentrations are required to describe the measurement data with only a single defect model. For example, when doping ceria with 10 mol% Y^{3+}, a single isolated defect model can only describe the data up to $\delta \approx 0.02$, whereas in the case of 20 mol% it is valid until $\delta \approx 0.03$. Here, with only 5 mol% Zr^{4+} a single model appears to adequately describe δ at least until $\delta \approx 0.04$.

The nonstoichiometry as a function of T and p_{O_2} may be modelled by fitting appropriate equilibrium constants from eqn (4) and (6) to the experimental data. To do so, the following site and charge relations for 4+ valence dopants and pure ceria[19] are needed:

$$\left[Ce_{Ce}^{\times}\right] = 1 - 2\delta - X \tag{8}$$

$$\left[O_O^{\times}\right] = 2 - \delta \tag{9}$$

$$2\left[V_O^{\bullet\bullet}\right] = \left[Ce'_{Ce}\right] \tag{10}$$

$$2\delta = \left[Ce'_{Ce}\right] + 2\left[\left(Ce'_{Ce}V_O^{\bullet\bullet}Ce'_{Ce}\right)^{\times}\right] \tag{11}$$

where X = 0.045 is the dopant concentration of Zr^{4+} in the case of CZO_5. Thus, the equilibrium constants K_1 for eqn (4) and K_2 for eqn (6) are given by:

$$K_1 = \frac{\left[Ce'_{Ce}\right]^2\left[V_O^{\bullet\bullet}\right]p_{O_2}{}^{1/2}}{\left[Ce_{Ce}^{\times}\right]^2\left[O_O^{\times}\right]} = \frac{4\left[V_O^{\bullet\bullet}\right]^3 p_{O_2}{}^{1/2}}{(1-2\delta-X)^2(2-\delta)} \tag{12}$$

$$K_2 = \frac{\left[\left(Ce'_{Ce}V_O^{\bullet\bullet}Ce'_{Ce}\right)^{\times}\right]}{\left[Ce'_{Ce}\right]^2\left[V_O^{\bullet\bullet}\right]} = \frac{\delta - \left[V_O^{\bullet\bullet}\right]}{4\left[V_O^{\bullet\bullet}\right]^3} \tag{13}$$

K_1 and K_2 can be determined through a least square minimization of eqn (12) and (13) with the experimental nonstoichiometry data. Results are summarized in Fig. 3(a) and (b) for CeO_2 and CZO_5, respectively. As expected, K_1 for CZO_5 is higher compared to that for CeO_2 because of its higher reduction extent. Additionally, the slope for CeO_2 is higher than that for CZO_5, indicating that its reduction enthalpy (at least at low δ where the reaction is dominated by K_1) is higher and consistent with Kuhn *et al.*[10] K_2 for CeO_2 is decreasing with increasing temperature meaning defect interactions become less predominant at higher temperatures. K_2 for CZO_5 does not show a meaningful trend and values are much smaller than for CeO_2 because defect associations are probably not significant under the conditions investigated. In fact, in the case of CZO_5 at 1573 K, the best fit of K_2 is orders of magnitude below the fits at higher temperatures. These findings directly support the conclusions drawn from Fig. 2, namely that a single isolated defect

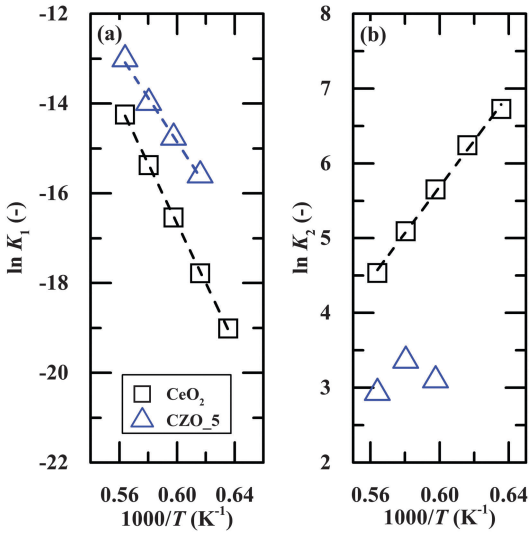

Fig. 3 Equilibrium constants *versus* inverse temperature for CeO_2 and CZO_5: (a) K_1; and (b) K_2. Dashed lines indicate linear dependence of K_1 and K_2 on $1000/T$ ($R^2 > 0.99$).

model appears to adequately describe the defect chemistry of CZO_5, whereas electron-vacancy associations should be additionally taken into account in the case of CeO_2. By fitting K_1 and K_2 over all experimental data, indicated by the lines in Fig. 2(a) and (b), it can be seen that the agreement is very good. When including both defect models, the RMS deviations of the fitted $\log p_{O_2}$ (*cf.* Fig. 2) are 0.013 and 0.005 in the case of CeO_2 and CZO_5, respectively. Both deviations are less than the uncertainty in the p_{O_2} setting, equal to 0.017. Considering only the isolated defect model (eqn (4)) the RMS deviations are 0.094 for CeO_2 and 0.038 for CZO_5. This reflects that defect associations are more important in the case of CeO_2 than in the case of CZO_5. The improvement in the RMS deviation for CZO_5 when including electron-vacancy associations may rather be a result of having an additional fitting parameter than having a more adequate physical model (*cf.* trend of K_2 for CZO_5 in Fig. 3(b)).

Based on computational investigations, Yang *et al.*[26] concluded that an oxygen vacancy is most likely created close to a Zr^{4+}-dopant which might serve as nucleation center for vacancy clustering. Based on these results, Kuhn *et al.*[10] proposed that the considerably smaller Zr^{4+}, compared with Ce^{4+}, prefers a 7-fold coordination (instead of 8-fold) with oxygen which can be achieved if an oxygen vacancy is created next to the smaller Zr^{4+} cation. Therefore, $(Zr_{Ce}^{\times}V_{O}^{\bullet\bullet})^{\bullet\bullet}$ instead of $(Ce'_{Ce}V_{O}^{\bullet\bullet}Ce'_{Ce})^{\times}$ associations were also tested, but this did not improve the isolated defect model within the δ-range investigated.

Thermodynamic properties

Thermodynamic properties, namely partial molar enthalpy (Δh_O), partial molar entropy (Δs_O) and partial molar Gibbs free energy (Δg_O), defined per mole of monoatomic oxygen, can be determined as a function of δ, temperature and p_{O_2} according to eqn (14) and (15).

$$\Delta g_O = \frac{1}{2}RT\ln p_{O_2} \tag{14}$$

$$\Delta g_O = \Delta h_O - T\Delta s_O \tag{15}$$

By combining eqn (14) and (15) it is clear that Δh_O and Δs_O as a function of δ can both be solved by determining the slope and intercept of $\ln p_{O_2}$ *versus* $1/T$ for a constant δ, as shown in eqn (16).

$$\frac{1}{2}\ln p_{O_2} = \frac{\Delta h_O}{RT} - \frac{\Delta s_O}{R}\bigg|_{\delta=\text{const.}} \tag{16}$$

Constant δ values are obtained by interpolating our defect models within the temperature range investigated (1573 K to 1773 K) and a slightly extrapolated p_{O_2} range (±20% of the measured $-\log p_{O_2}$ range). Results of Δh_O and Δs_O *versus* δ are shown in Fig. 4 and 5, respectively, for CeO_2 (open squares) and CZO_5 (open triangles) measurements from this work. For reference we have included CeO_2 data of Panlener *et al.*,[4] Campserveux *et al.*,[17] Bevan *et al.*[5] and Sørensen.[16] Additionally, measurements of CZO_5 by Kuhn *et al.*[10] and Hao *et al.*[12] are indicated by closed and crossed triangles, respectively. Measurements of 20 mol% Zr^{4+} doped CeO_2 (CZO_20) by Kuhn *et al.*[10] and Hao *et al.*[12] are indicated by closed circles and crossed circles, respectively. In general, it can be observed that Δh_O increases with increasing dopant concentration. This is expected due to the ease with which Zr^{4+} doped ceria reduces compared to pure ceria.

Towards higher δ, the Δh_O values are in good agreement with literature data of CeO_2[4,5,16,17] and CZO_5.[10,12] However, at lower δ, they deviate. The same trend can be observed for Δs_O.

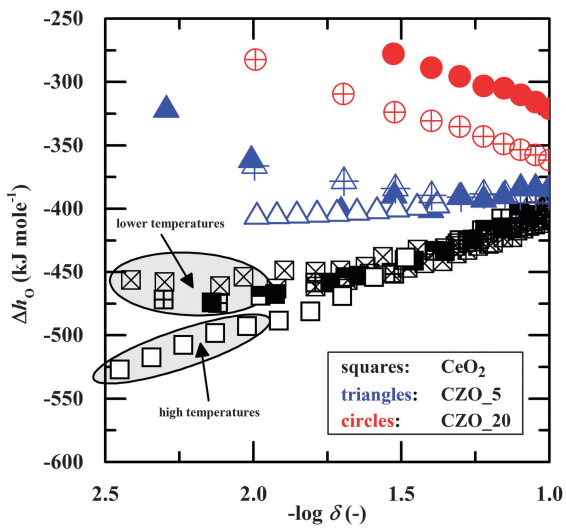

Fig. 4 Partial molar enthalpy of CeO_2 (open squares) and CZO_5 (open triangles) as a function of δ and a comparison to literature data of CeO_2 (Panlener *et al.*:[4] closed squares, Campserveux *et al.*:[17] diagonally crossed squares, Bevan *et al.*:[5] half closed squares, Sørensen:[16] crossed squares), CZO_5 (Kuhn *et al.*:[10] closed triangles, Hao *et al.*:[12] crossed triangles) and CZO_20 (Kuhn *et al.*:[10] closed circles, Hao *et al.*:[12] crossed circles).

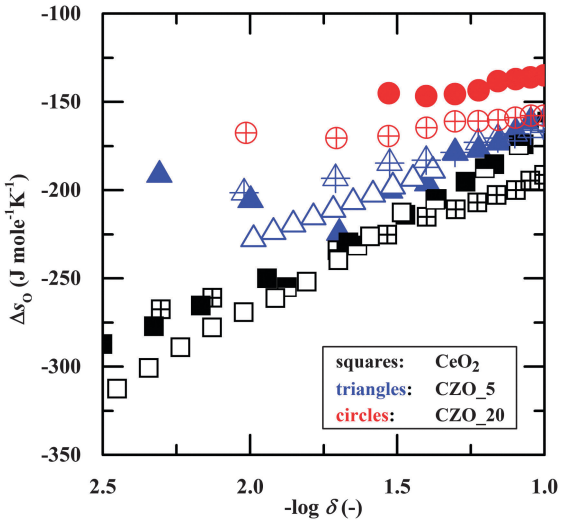

Fig. 5 Partial molar entropy of CeO_2 (open squares) and CZO_5 (open triangles) as a function of δ and a comparison to literature data of CeO_2 (Panlener *et. al.*:[4] closed squares, Bevan *et al.*:[5] half closed squares, Sørensen:[16] crossed squares), CZO_5 (Kuhn *et al.*:[10] closed triangles, Hao *et al.*:[12] crossed triangles) and CZO_20 (Kuhn *et al.*:[10] closed circles, Hao *et al.*:[12] crossed circles).

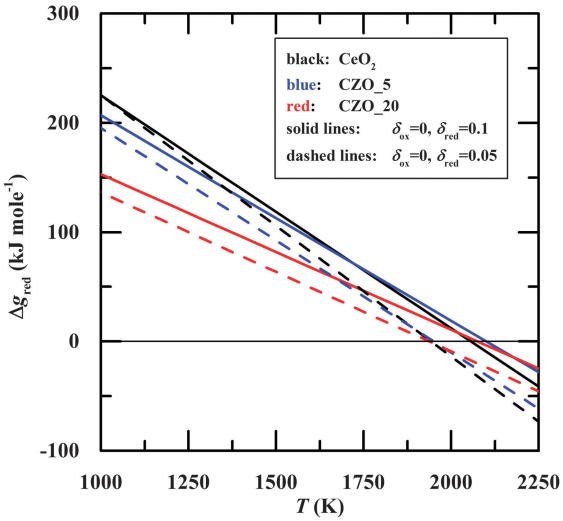

Fig. 6 Gibbs free energy change *versus* temperature for the reduction of CeO_2 (black), CZO_5 (blue) and CZO_20 (red) from δ_{ox} = 0 to δ_{red} = 0.1 (solid lines) and δ_{ox} = 0 to δ_{red} = 0.05 (dashed lines).

Deviations can be attributed primarily to different measurement temperatures and to a lesser extent to differences in nonstoichiometry measurements. For example, the literature data shown in Fig. 4 and 5 were calculated based on measurements below 1573 K[5,10,16,17] or as an average of measurements at higher (>1573 K) and lower temperatures (<1573 K),[4,12] whereas values of this work are based on measurements only above 1573 K. Although it is often assumed that Δh_O and Δs_O are independent of temperature, this simplifying assumption is not always valid. For example, a temperature dependence of Δh_O is observed for the case of CeO_2 where two reactions dictate the defect chemistry. The degree of dependence varies in accordance with the magnitude of K_2 in regards to K_1. Sørensen[16] has showed that the slope of Δg_O *vs.* T (see eqn (15)) is constant at $T < 1623$ K and $\delta < 0.08$, but decreases at higher temperatures due to the formation of sub-phases. The more negative Δh_O values at low δ from this work are in agreement with Sørensen.[16] Deviations in the measurements of CZO_5 can be additionally attributed to differences in Zr^{4+} dopant concentrations. For example, in this work the dopant concentration is 4.5 mol% compared to 5.2 mol% in the work of Hao *et al.*[12]

The reduction of nonstoichiometric ceria is represented by:

$$\frac{1}{\delta_{red}-\delta_{ox}}CeO_{2-\delta_{ox}} = \frac{1}{\delta_{red}-\delta_{ox}}CeO_{2-\delta_{red}} + \frac{1}{2}O_2 \qquad (17)$$

The standard Gibbs free energy change of eqn (17), Δg_{red}, can be calculated by integrating Δg_O over the range of δ:[16]

$$\Delta g_{red} = \frac{\int_{\delta_{red}}^{\delta_{ox}} \Delta g_O d\delta}{\delta_{red}-\delta_{ox}} \qquad (18)$$

where δ_{ox} is the nonstoichiometry before reduction and δ_{red} is the nonstoichiometry after reduction. Δg_{red} as a function of temperature for the reduction of CeO_2, CZO_5, and CZO_20 from δ_{ox} = 0 to δ_{red} = 0.05 (dashed lines) and from δ_{ox} = 0 to δ_{red} = 0.1 (solid lines) is shown in Fig. 6. For all materials, the reduction at standard pressure is thermodynamically favorable ($\Delta g_{red} < 0$) at $T > 1950$ K for δ_{red} = 0.05 and at $T > 2100$ K for δ_{red} = 0.1. At lower temperatures, where $\Delta g_{red} > 0$, reduction would only proceed if additional work is performed to the system, *e.g.* lowering p_{O_2} by vacuum pumping or flushing with inert gas. Therefore, this implies that at lower temperatures (<2000 K), CZO_20 can be reduced more easily compared to CZO_5 and CeO_2, which is related to its less negative Δh_O and consistent with experimental observations. For all materials, a higher Δg_{red} for δ_{red} = 0.1 compared to δ_{red} = 0.05 is related to the increasing Δs_O with increasing δ (*cf.* Fig. 5).

The oxidation of nonstoichiometric ceria and doped ceria with H_2O is described by:

$$\frac{1}{\delta_{red}-\delta_{ox}}CeO_{2-\delta_{red}} + H_2O = \frac{1}{\delta_{red}-\delta_{ox}}CeO_{2-\delta_{ox}} + H_2 \qquad (19)$$

Δg_{ox}, Δg_{H_2O}, and $\Delta g_{ox,H_2O}$ are the standard Gibbs free energy change of ceria oxidation with oxygen ($-\Delta g_{red}$), of water dissociation, and of ceria oxidation with H_2O (eqn (19)). Thus, $\Delta g_{ox,H_2O} = \Delta g_{ox} + \Delta g_{H_2O}$, where Δg_{H_2O} is obtained from NIST-JANAF thermochemical tables and $\Delta g_{ox} = -\Delta g_{red}$. Calculations indicate that oxidation with H_2O becomes thermodynamically less favorable as the Zr^{4+} concentration increases. This is shown in Fig. 7, where $\Delta g_{ox,H_2O}$ of CeO_2 (black), CZO_5 (blue), and CZO_20 (red) is plotted as a function of temperature for the oxidation with H_2O from δ_{red} = 0.1 to δ_{ox} = 0 (solid lines) and δ_{red} = 0.05 to δ_{ox} = 0 (dashed lines). $\Delta g_{ox,H_2O}$ is negative at $T \leq$ 1200 K for CeO_2, at $T \leq 1000$ K for CZO_5, and at $T \leq 500$ K for CZO_20. Above the mentioned temperatures, oxidation is

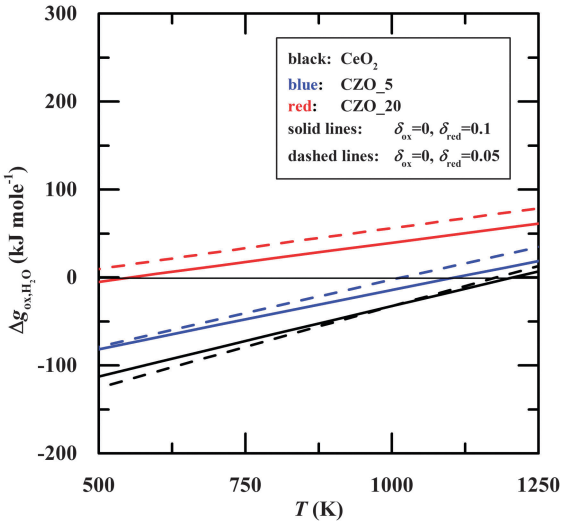

Fig. 7 Gibbs free energy change *versus* temperature for the oxidation of CeO_2 (black), CZO_5 (blue), and CZO_20 (red) with H_2O from δ_{red} = 0.1 to δ_{ox} = 0 (solid lines) and δ_{red} = 0.05 to δ_{ox} = 0 (dashed lines).

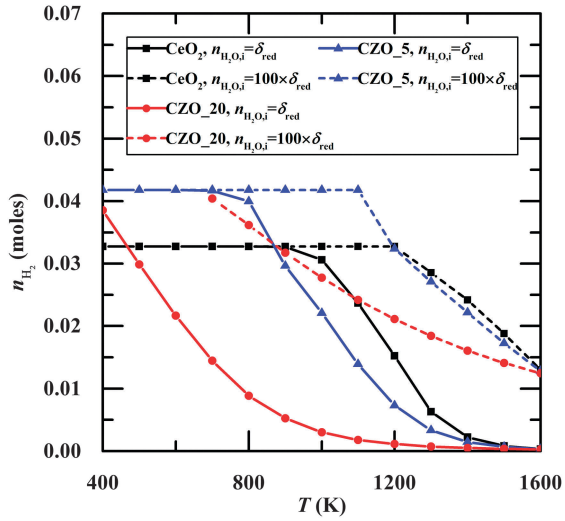

Fig. 8 Molar amount of H_2 produced by oxidation of CeO_2 (black), CZO_5 (blue) and CZO_20 (red) with H_2O as a function of temperature assuming $n_{H_2O,i}$ = δ_{red} (solid lines) and 100 × δ_{red} (dashed lines) where δ_{red} is the nonstoichiometry achieved after reduction at T_{red} = 1773 K and p_{O_2} = 2.3 × 10^{-4} atm (δ_{red} = 0.0328 for CeO_2, δ_{red} = 0.0417 for CZO_5, and δ_{red} = 0.0725 for CZO_20).

thermodynamically favorable only if additional work is added to the system.

By combining the reaction equilibrium constant of water dissociation (K_W)

$$K_W = \frac{n_{H_2} p_{O_2}{}^{1/2}}{\left(n_{H_2O,i} - n_{H_2}\right)} \tag{20}$$

with eqn (14), equilibrium H_2 yields can be calculated according to:

$$\Delta g_O\left(\delta_{ox} = \delta_{red} - n_{H_2}\right) = RT \ln\left[\frac{K_W\left(n_{H_2O,i} - n_{H_2}\right)}{n_{H_2}}\right] \tag{21}$$

where n_{H_2} is the molar amount of H_2 produced at equilibrium per mole oxide, and $n_{H_2O,i}$ is the initial molar amount of H_2O in the system per mole oxide. n_{H_2} is obtained by iteratively solving eqn (21) and is shown in Fig. 8 *versus* temperature for CeO_2 (black), CZO_5 (blue), and CZO_20 (red). $n_{H_2O,i}$, is set equal to δ_{red} (solid lines) and 100 × δ_{red} (dashed lines), where δ_{red} is the nonstoichiometry achieved after reduction at T_{red} = 1773 K and p_{O_2} = 2.3 × 10^{-4} atm. The calculations reaffirm that the oxidation with H_2O becomes thermodynamically less favorable with increasing Zr^{4+} dopant concentrations. For example, for $n_{H_2O,i}$ = δ_{red}, maximum n_{H_2} is reached at $T \leq$ 900 K for CeO_2, $T \leq$ 700 K for CZO_5, and $T <$ 400 K for CZO_20. If $n_{H_2O,i}$ is increased by a factor of hundred, these oxides can be oxidized at higher temperatures but at the expense of heating excess H_2O. In this case, maximum n_{H_2} is obtained at as high as 1200 K for CeO_2, 1100 K for CZO_5, and 500 K for CZO_20. For CZO_20, n_{H_2} is only shown up to 0.042 moles because Δh_O and Δs_O are not available at $\delta \leq$ 0.03. Because Δh_O and Δs_O of CeO_2 and CZO_5 are not measured over the range δ = 0 to 0.1, they are assumed to be constant for low δ and taken as the average from literature data[4,5,10,16,17] for high δ.

Efficiency analysis

The theoretical solar-to-fuel energy conversion efficiency ($\eta_{solar\text{-}to\text{-}fuel}$) for the case of hydrogen production is defined as:

$$\eta_{solar\text{-}to\text{-}fuel} = \frac{HHV_{H_2} n_{H_2}}{Q_{input,min}} \tag{22}$$

where HHV_{H_2} = 285.5 kJ mol^{-1} is the higher heating value of H_2. $Q_{input,min}$ is the minimum input of energy required to produce n_{H_2} and comprises the solar process heat for driving the reduction, for heating the redox material from T_{ox} to T_{red}, and for generating steam at T_{ox}, as well as the equivalent minimum work to drive the reduction for the case of $\Delta g_{red} > 0$. Assuming no heat recuperation between the redox steps,

$$Q_{input,min} = \frac{1}{\eta_{absorption}} \cdot \left[\Delta h_{red}(\delta_{red} - \delta_{ox}) + \int_{T_{ox}}^{T_{red}} c_p \mathrm{d}T + \Delta h_{H_2O}\big|_{298K \to T_{ox}} n_{H_2O,i} + \frac{\Delta g_{red}}{\eta_{Carnot}}(\delta_{red} - \delta_{ox})\right] \tag{23}$$

where Δh_{red} is the enthalpy change of the reduction (eqn (17)),

$$\Delta h_{red} = \frac{\int_{\delta_{ox}}^{\delta_{red}} \Delta h_O \mathrm{d}\delta}{\delta_{red} - \delta_{ox}} \tag{24}$$

$\Delta h_{H_2O}\big|_{298K \to T_{ox}}$ is the thermal energy required to heat H_2O from ambient temperature to T_{ox} (obtained from NIST-JANAF tables), $n_{H_2O,i}$ is the initial molar amount of H_2O determined by eqn (21), and c_p is the specific heat capacity of pure ceria.[27] The excess H_2O needed is calculated for n_{H_2} approaching δ_{red}. Note that the maximum $\eta_{solar\text{-}to\text{-}fuel}$ may not be attained by completely re-oxidizing the material, as shown by Chueh *et al.*[28] and Furler *et al.*,[29] but an

overall optimization routine is outside the scope of this work. Due to the low dopant concentration of Zr^{4+}, c_p of CZO_5 and CZO_20 are assumed to be identical to that of pure CeO_2. $Q_{input,min}$ is assumed to be delivered by concentrated solar energy. The solar absorption efficiency ($\eta_{absorption}$) for a blackbody cavity-receiver is given by:[30]

$$\eta_{absorption} = 1 - \frac{\sigma T_{red}^4}{IC} \tag{25}$$

where σ is the Stefan–Boltzmann constant, $I = 1$ kW m^{-2} the direct normal irradiation (DNI) and $C = 2000$ the solar flux concentration ratio. The fourth term in eqn (23) is the minimum work required to drive the reduction at conditions for which $\Delta g_{red} > 0$; when $\Delta g_{red} \leq 0$ this term is omitted. η_{Carnot} is the efficiency of an ideal heat engine converting solar heat at T_{red} to work.[30]

A contour plot of $\eta_{solar\text{-}to\text{-}fuel}$ shown as a function of δ_{red} and T_{ox} is shown in Fig. 9 for CeO_2 (a) and CZO_5 (b) respectively. $p_{O_2} = 10^{-6}$ atm is assumed for the efficiency calculations resulting in reduction temperatures of 1744 K for CeO_2 and 1741 K for CZO_5 needed to reach $\delta_{red} = 0.1$ and 1564 K and 1510 K respectively to reach $\delta_{red} = 0.02$. It is shown that the maximum efficiency for CeO_2 is slightly higher compared to CZO_5. $\eta_{solar\text{-}to\text{-}fuel}$ is slightly greater than 17% at $\delta_{red} = 0.1$ ($T_{ox} = 1050$ K) for CeO_2 and slightly greater than 16% at $\delta_{red} = 0.1$ ($T_{ox} = 880$ K) for CZO_5. Simply stated, the energy savings during reduction of CZO_5 cannot compensate the additional energy inputs due to the less favorable re-oxidation with H_2O (lower T_{ox} and/or higher $n_{H_2O,i}$ compared to CeO_2). In general $\eta_{solar\text{-}to\text{-}fuel}$ rapidly decreases towards higher T_{ox} as the re-oxidation with H_2O gets thermodynamically less favorable and an increasing amount of excess steam has to be heated in order to fully oxidize the reduced material. Towards lower T_{ox}, $\eta_{solar\text{-}to\text{-}fuel}$ decreases as the temperature difference between oxidation and reduction increases and towards lower δ_{red} it decreases as the amount of H_2 produced (equal to δ_{red}) decreases compared to the sensible energy required to heat the oxide. Qualitatively these results are in agreement with calculations reported in literature for pure ceria,[7,31,32] and indicate the tradeoffs between an isobaric redox cycle driven by temperature swing and an isothermal redox cycle driven by pressure swing. Heat recovery, not accounted for in Fig. 9, can significantly boost $\eta_{solar\text{-}to\text{-}fuel}$.[7] When heat recovery is used for generating steam at T_{ox}, $\eta_{solar\text{-}to\text{-}fuel}$ peaks at 19% for CeO_2 and 18% for CZO_5. If, in addition, heat recovery is used to heat the redox material from T_{ox} to T_{red}, $\eta_{solar\text{-}to\text{-}fuel}$ peaks at 41% and 44% for CeO_2 and CZO_5, respectively. Results for CZO_20 are not shown because thermodynamic data are not available at $\delta \leq 0.03$ and also because calculations always predict maximum $\eta_{solar\text{-}to\text{-}fuel}$ at lowest T_{ox} (400 K) and highest δ_{red} (0.1).

Maximum $\eta_{solar\text{-}to\text{-}fuel}$ as a function of p_{O_2} is shown in Fig. 10 for CeO_2 (solid lines), CZO_5 (dashed lines) and CZO_20 (dotted lines) where $\delta_{red} = 0.1$ (a) and $\delta_{red} = 0.05$ (b). Additionally, T_{red} where maximum $\eta_{solar\text{-}to\text{-}fuel}$ is obtained is shown in Fig. 10. Estimates of

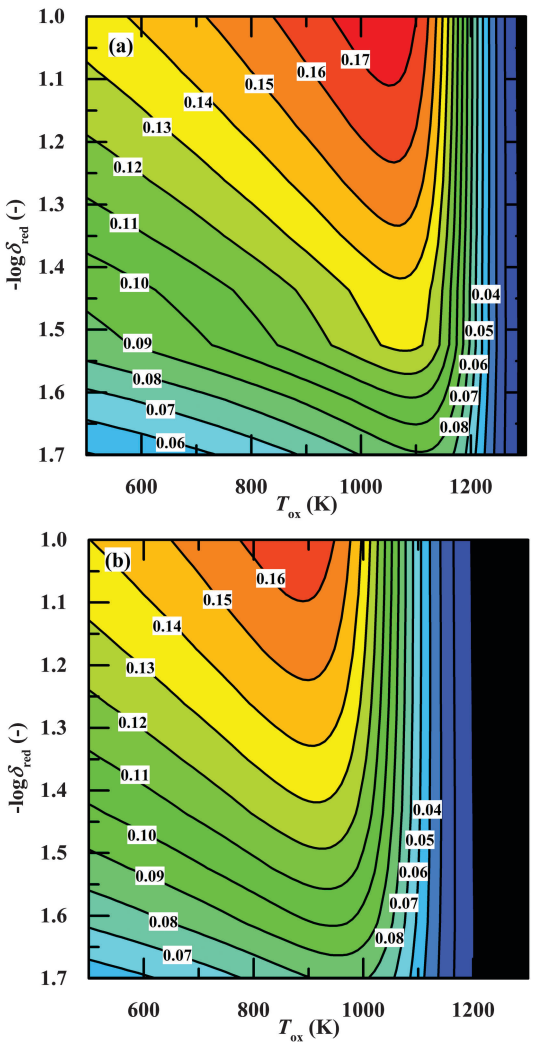

Fig. 9 $\eta_{solar\text{-}to\text{-}fuel}$ shown as contour lines for CeO_2 (a) and CZO_5 (b) as a function of δ_{red} and T_{ox} assuming reduction at $p_{O_2} = 10^{-6}$ atm and subsequent complete re-oxidation with steam.

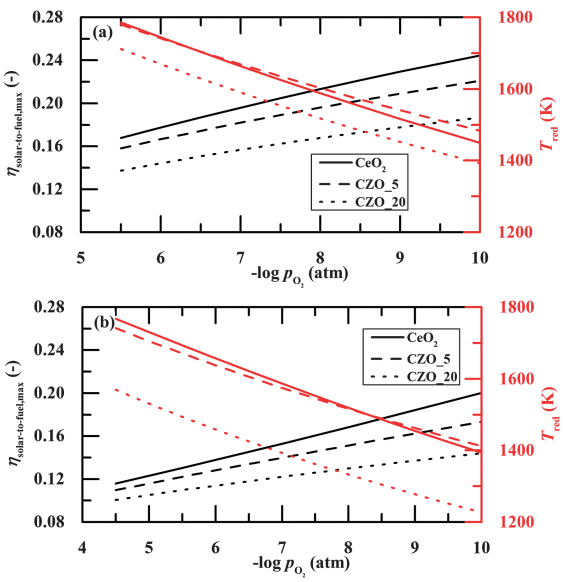

Fig. 10 Maximum $\eta_{solar\text{-}to\text{-}fuel}$ and T_{red} *versus* p_{O_2} for CeO_2 (solid lines), CZO_5 (dashed lines) and CZO_20 (dotted lines) assuming $\delta_{red} = 0.1$ (a) and $\delta_{red} = 0.05$ (b).

T_{red} of CZO_20 were calculated according to the methodology described by Yang *et al.*[33] using the thermodynamic data of Kuhn *et al.*[10] It is observed that CeO_2 shows the highest $\eta_{solar\text{-}to\text{-}fuel}$ under all conditions investigated and CZO_20 shows the lowest $\eta_{solar\text{-}to\text{-}fuel}$. Although CZO_20 reduces at substantially lower temperatures compared to CZO_5 and CeO_2, the lower energy input during reduction cannot compensate the higher energy input during oxidation with H_2O. In general, $\eta_{solar\text{-}to\text{-}fuel}$ increases with decreasing p_{O_2}, meaning less energy is required to reduce the oxide by lowering p_{O_2} compared to increasing T_{red}.

Conclusions

Oxygen nonstoichiometry measurements of Zr^{4+} doped ceria at elevated temperatures presented in this work are largely in agreement with the trends observed in works performed at lower temperatures (<1573 K), namely: for a given T_{red} and p_{O_2} the reduction extent increases and the reduction enthalpy decreases with increasing Zr^{4+} concentration. Extracted thermodynamic properties are also largely in agreement with previous data, but they deviate at low nonstoichiometries especially for the case of pure ceria. This is likely due to the fact that they are slightly temperature dependent, especially at higher temperatures (>1623 K) where different sub-phases can be expected.[16] Interestingly, in the case of 5 mol% Zr^{4+} doped ceria, a single defect model is capable of describing the nonstoichiometry data over the entire measurement range (δ = 0.01 to 0.04) and therefore the thermodynamic properties can be assumed to be independent of temperature. This is an important distinction when extrapolating nonstoichiometries to conditions that have not yet been measured experimentally.[33] Although the nonstoichiometry increases with increasing Zr^{4+} dopant concentration, oxidation with steam becomes thermodynamically less favorable and has to be conducted at lower temperatures or with excess amounts of steam. This ultimately results in lower theoretical solar-to-fuel energy conversion efficiencies compared to that for pure ceria. Therefore, when screening potential redox materials it is important to consider both steps of the cycle, *i.e.* the materials ability to release lattice oxygen and its oxidation potential with H_2O and CO_2. We have assumed that reduction and oxidation are driven to completion, but maximum efficiencies may be found at lower extents. In general, when we compare with the thermodynamic properties of pure ceria, a relatively lower partial molar enthalpy and a relatively higher partial molar entropy are desired, resulting in $\Delta g_{red} < 0$ at lower T_{red} and $\Delta g_{ox,H_2O} < 0$ at higher T_{ox}, which in turn yields a smaller temperature swing between the redox steps. Besides thermodynamic aspects, fast reaction kinetics and long term chemical and morphological stability are obviously essential.

Nomenclature

C	Flux concentration ratio of incident radiation (—)
$Ce_{Ce}^{\times}$	Cerium atom on cerium lattice site
Ce'_{Ce}	Electron localized on cerium lattice site
$(Ce'_{Ce}V_O^{\bullet\bullet}Ce'_{Ce})^{\times}$	Oxygen vacancy–polaron association
c_p	Heat capacity of CeO_2 (kJ mol^{-1} K^{-1})
Δg_{H_2O}	Standard Gibbs free energy change of H_2O dissociation (kJ mol^{-1})
Δg_O	Partial molar free energy (kJ mol^{-1})
Δg_{ox}	Standard Gibbs free energy change of ceria oxidation (with O_2) (kJ mol^{-1})
$\Delta g_{ox,H_2O}$	Standard Gibbs free energy change of ceria oxidation (with H_2O) (kJ mol^{-1})
Δg_{red}	Standard Gibbs free energy change of ceria reduction (kJ mol^{-1})
Δh_{H_2O}	Energy to heat water (kJ mol^{-1})
HHV_{H_2}	Higher heating value of H_2 (kJ mol^{-1})
Δh_O	Partial molar enthalpy (kJ mol^{-1})
Δh_{red}	Enthalpy change of reduction (kJ mol^{-1})
I	Normal beam insolation (W m^{-2})
K_1	Ideal solution model equilibrium constant (—)
K_2	Defect interaction model equilibrium constant (—)
K_W	H_2O dissociation equilibrium constant (—)
M_O	Molar mass of O (g mol^{-1})
m_s	Weight of reactive sample (mg)
M_s	Molar mass of reactive sample (g mol^{-1})
Δm_s	Relative weight loss of reactive sample (—)
n_{H_2}	Molar amount of H_2 at equilibrium (mol)
$n_{H_2O,i}$	Initial molar amount of H_2O (mol)
$O_O^{\times}$	Oxygen atom on oxygen lattice site
p_{O_2}	Oxygen partial pressure (atm)
$Q_{input,min}$	Minimum amount of input energy to produce H_2 (kJ mol^{-1})
R	Universal gas constant (J mol^{-1} K^{-1})
Δs_O	Partial molar entropy (J mol^{-1} K^{-1})
T	Temperature (K)
T_{ox}	Oxidation temperature (K)
T_{red}	Reduction temperature (K)
$V_O^{\bullet\bullet}$	Doubly ionized oxygen vacancy
X	Molar dopant concentration of Zr^{4+} (—)
α	Stoichiometric coefficient of H_2O (—)
β	Stoichiometric coefficient of CO_2 (—)
δ	Degree of oxygen nonstoichiometry (—)
δ_{ox}	Degree of oxygen nonstoichiometry after oxidation (—)
δ_{red}	Degree of oxygen nonstoichiometry after reduction (—)
$\eta_{absorption}$	Solar absorption efficiency (—)
η_{Carnot}	Carnot efficiency (—)
$\eta_{solar\text{-}to\text{-}fuel}$	Solar-to-fuel energy conversion efficiency (—)
σ	Stefan–Boltzmann constant (W m^{-2} K^{-4})

Acknowledgements

We gratefully acknowledge the financial support by the Swiss Competence Center Energy & Mobility, the Helmholtz-Gemeinschaft Deutscher Forschungszentren (Virtuelles Institut SolarSyngas),

and the European Research Council under the European Union's ERC Advanced Grant (SUNFUELS – no. 320541).

References

1 G. P. Smestad and A. Steinfeld, *Ind. Eng. Chem. Res.*, 2012, **51**, 11828–11840.
2 M. Romero and A. Steinfeld, *Energy Environ. Sci.*, 2012, **5**, 9234–9245.
3 W. C. Chueh and S. M. Haile, *Philos. Trans. R. Soc., A*, 2010, **368**, 3269–3294.
4 R. J. Panlener, R. N. Blumenthal and J. E. Garnier, *J. Phys. Chem. Solids*, 1975, **36**, 1213–1222.
5 D. J. M. Bevan and J. Kordis, *J. Inorg. Nucl. Chem.*, 1964, **26**, 1509–1523.
6 J. R. Scheffe and A. Steinfeld, *Mater. Today*, 2014, **17**, 341–348.
7 J. R. Scheffe and A. Steinfeld, *Energy Fuels*, 2012, **26**, 1928–1936.
8 J. R. Scheffe, R. Jacot, G. R. Patzke and A. Steinfeld, *J. Phys. Chem. C*, 2013, **117**, 24104–24114.
9 S. Abanades, A. Legal, A. Cordier, G. Peraudeau, G. Flamant and A. Julbe, *J. Mater. Sci.*, 2010, **45**, 4163–4173.
10 M. Kuhn, S. R. Bishop, J. L. M. Rupp and H. L. Tuller, *Acta Mater.*, 2013, **61**, 4277–4288.
11 F. Call, M. Roeb, M. Schmücker, H. Bru, D. Curulla-Ferre, C. Sattler and R. Pitz-Paal, *Am. J. Anal. Chem.*, 2013, **4**, 37.
12 Y. Hao, C.-K. Yang and S. M. Haile, *Chem. Mater.*, 2014, **26**, 6073–6082.
13 Q.-L. Meng, C.-i. Lee, T. Ishihara, H. Kaneko and Y. Tamaura, *Int. J. Hydrogen Energy*, 2011, **36**, 13435–13441.
14 A. Le Gal, S. Abanades, N. Bion, T. Le Mercier and V. Harlé, *Energy Fuels*, 2013, **27**, 6068–6078.
15 P. R. Shah, T. Kim, G. Zhou, P. Fornasiero and R. J. Gorte, *Chem. Mater.*, 2006, **18**, 5363–5369.
16 O. T. Sørensen, *J. Solid State Chem.*, 1976, **18**, 217–233.
17 J. Campserveux and P. Gerdanian, *J. Chem. Thermodyn.*, 1974, **6**, 795–800.
18 B. Iwasaki and T. Katsura, *Bull. Chem. Soc. Jpn.*, 1971, **44**, 1297–1301.
19 T. Otake, H. Yugami, K. Yashiro, Y. Nigara, T. Kawada and J. Mizusaki, *Solid State Ionics*, 2003, **161**, 181–186.
20 S. R. Bishop, K. L. Duncan and E. D. Wachsman, *Electrochim. Acta*, 2009, **54**, 1436–1443.
21 M. Mogensen, N. M. Sammes and G. A. Tompsett, *Solid State Ionics*, 2000, **129**, 63–94.
22 L. J. Gauckler, M. Gödickemeier and D. Schneider, *J. Electroceram.*, 1997, **1**, 165–172.
23 T. Kobayashi, S. Wang, M. Dokiya, H. Tagawa and T. Hashimoto, *Solid State Ionics*, 1999, **126**, 349–357.
24 S. Wang, H. Inaba, H. Tagawa and T. Hashimoto, *J. Electrochem. Soc.*, 1997, **144**, 4076–4080.
25 S. Wang, H. Inaba, H. Tagawa, M. Dokiya and T. Hashimoto, *Solid State Ionics*, 1998, **107**, 73–79.
26 Z. Yang, T. K. Woo and K. Hermansson, *J. Chem. Phys.*, 2006, **124**, 224704.
27 Y. S. Touloukian, DTIC Document, 1966.
28 W. C. Chueh, C. Falter, M. Abbott, D. Scipio, P. Furler, S. M. Haile and A. Steinfeld, *Science*, 2010, **330**, 1797–1801.
29 P. Furler, J. Scheffe, M. Gorbar, L. Moes, U. Vogt and A. Steinfeld, *Energy Fuels*, 2012, **26**, 7051–7059.
30 A. Steinfeld and R. Palumbo, *Encyclopedia of Physical Science and Technology*, 2001, pp. 237–256.
31 J. R. Scheffe, D. Weibel and A. Steinfeld, *Energy Fuels*, 2013, **27**, 4250–4257.
32 I. Ermanoski, J. E. Miller and M. D. Allendorf, *Phys. Chem. Chem. Phys.*, 2014, **16**, 8418–8427.
33 C.-K. Yang, Y. Yamazaki, A. Aydin and S. M. Haile, *J. Mater. Chem. A*, 2014, **2**, 13612–13623.

